Draft version December 11, 2006
Preprint typeset using LaTeX style emulateapj v. 10/09/06

DETONATING FAILED DEFLAGRATION MODEL OF THERMONUCLEAR SUPERNOVAE II. COMPARISON TO OBSERVATIONS

Daniel Kasen[1,2], Tomasz Plewa[3,4]

Draft version December 11, 2006

ABSTRACT

We develop and demonstrate the methodology of testing multi-dimensional supernova models against observations by studying the properties of one example of the detonation from failed deflagration (DFD) explosion model of thermonuclear supernovae. Using time-dependent multi-dimensional radiative transfer calculations, we generate the synthetic broadband optical light curves, near-infrared light curves, color evolution curves, full spectral time-series, and spectropolarization of the model, as seen from various viewing angles. All model observables are critically evaluated against examples of well-observed, standard Type Ia supernovae (SNe Ia). We explore the consequences of the intrinsic model asphericity by studying the dependence of the model emission on viewing angle, and by quantifying the resulting dispersion in (and internal correlations between) various model observables. These *statistical* properties of the model are also evaluated against those of the available observational sample of SNe Ia. On the whole, the DFD model shows good agreement with a broad range of SN Ia observations. Certain deficiencies are also apparent, and point to further developments within the basic theoretical framework. We also identify several intriguing orientation effects in the model which suggest ways in which the asphericity of SNe Ia may contribute to their photometric and spectroscopic diversity and, conversely, how the relative homogeneity of SNe Ia constrains the degree of asymmetry allowable in the models. The comprehensive methodology adopted in this work proves an essential component of developing and validating theoretical supernova models, and helps motivate and clearly define future directions in both the modeling and the observation of SNe Ia.

Subject headings: hydrodynamics — radiative transfer — spectropolarimetry — supernovae:general

1. INTRODUCTION

The critical assessment of theories of thermonuclear, or Type Ia, supernova (SN) explosions must ultimately involve not only the modeling of the complex 3-dimensional physics characterizing the explosion process itself, but also a comprehensive treatment of the multi-dimensional radiative transfer physics determining the emission from the ejected stellar material over the months and years following explosion, thereby allowing the model to be tested by direct comparison to a broad range of supernova observations, such as light curves, spectra and spectropolarization, the aim being to reproduce the essential features of the observational sample, within the framework of a certain theoretical paradigm, and with the minimum number of free parameters and assumptions.

Most theories of Type Ia supernova (SN Ia) explosions begin with the assumption that these events represent the thermonuclear disruption of carbon-oxygen white dwarfs, typically near the Chandrasekhar limit. Despite several uncertainties concerning the structure of the progenitor star and the precise conditions leading to its ignition, complex multi-physics codes have been used to simulate the hydrodynamics and turbulent nuclear combustion leading to the unbinding of the white dwarf. Nuclear burning typically lasts for up to 5 sec after ignition; the stellar material ejected in the explosion reaches the free-expansion phase ~ 1 minute later. At this time, the model output (i.e., the density, velocity, and compositional structure of the SN ejecta) may be fed into detailed radiative transfer codes for calculation of the synthetic model spectra, light curves and polarization.

The diagnostic value of such transfer calculations in assessing the model predictions is impressive. Light curve observations constrain the explosion energy, the total ejected mass, and the amount and distribution of the synthesized radioactive products (in particular ^{56}Ni) which power the SN light curve. Spectroscopic observations constrain the ejecta velocity scale, thermal state and chemical stratification. Spectropolarization observations constrain asymmetries and inhomogeneities in the ejecta density and compositional structure. Given the extreme complexity of the underlying phenomenon, no single measure can be used to establish the viability of a SN explosion model, rather one must consider this broad set of model observables as a whole.

Inevitably, the comparison of model and observation involves a number of important uncertainties, including the physical approximations and geometrical simplifications adopted in the theoretical calculations, as well as errors in the observations of SNe, their distances and the degree of dust extinction. Nevertheless, radiative transfer studies of 1-dimensional (1D) SN Ia models have already provided important insights into the nature and theory of these objects. Höflich & Khokhlov (1996), for example, synthesized light curves for a wide range of 1D theoretical models, including deflagrations, pulsed detonations and delayed-detonations, and compared the results directly to observations. The spectroscopic prop-

[1] Allan C. Davis Fellow, Department of Physics and Astronomy, Johns Hopkins University, Baltimore, MD 21218
[2] Space Telescope Science Institute, Baltimore, MD 21218
[3] Center for Astrophysical Thermonuclear Flashes, University of Chicago, 5640 South Ellis Avenue, Chicago, IL 60637
[4] Department of Astronomy & Astrophysics, University of Chicago, 5640 South Ellis Avenue, Chicago, IL 60637

erties of the parameterized 1D deflagration model w7 of Nomoto et al. (1984) have been frequently evaluated against observations (Branch et al. 1985; Harkness 1991; Jeffery et al. 1992; Nugent et al. 1997; Lentz et al. 2001; Baron et al. 2006). In addition, the synthetic light curves and spectra of 1D delayed-detonation models have been studied in great detail, both in the optical and near infrared (Höflich 1995; Höflich et al. 1995, 2002; Wheeler et al. 1998). All of these studies, by specifying the particular successes and failures of the models, have helped define the basic features required of any viable theory of SNe Ia. To date, however, there does not exist a self-consistent, fully unparameterized SN Ia model that satisfies all the observable properties of the class.

With the advance of computing power, more realistic explosion models of SNe Ia have shown that multi-dimensional effects likely play an essential role in the explosion process (e.g., Khokhlov 1994; Reinecke et al. 2002). Corresponding advances in the observations, in particular polarization measurements, have given direct evidence that the ejecta of SNe Ia are not entirely spherically symmetric (Howell et al. 2001; Wang et al. 2003; Leonard et al. 2005; Chornock et al. 2006). The validation of SN models faces new and interesting challenges once multi-dimensional scenarios are considered. Although one can always study the gross, angle-averaged properties of aspherical models using 1D transfer codes (e.g., Blinnikov et al. 2006), ultimately multi-dimensional transfer calculations are needed to retain the full geometry of the problem. In that way we can study how the model properties depend on viewing angle, and quantify the resulting dispersion in (and internal correlations between) the various model observables. Such *statistical* properties of the models may then also be evaluated against those of the available observational sample of SNe Ia.

In this paper, we develop and demonstrate such a methodology for testing multi-dimensional supernova models by studying the observable properties of one example of the (axisymmetric) detonating-failed-deflagration (DFD) model of SNe Ia (Plewa 2006, hereafter Paper I). Using the multi-dimensional time-dependent radiative transfer code `SEDONA`, we calculate the full time evolution (day 2 to day 80 after explosion) of the emergent model spectrum as seen from various viewing angles. Broadband $UBVRIJHK$ light curves are then generated by convolving the spectral series with the appropriate filter transmission profiles. The intrinsic asymmetry of the model is studied by calculating synthetic spectropolarimetry and by examining the dependence of all model observables on orientation. The high spectral resolution of the calculations allows us to study individual absorption features in the synthetic spectra, and in particular the level of line polarization and the temporal evolution of line Doppler shifts. All model properties are critically contrasted with representative examples of normal SNe Ia.

Our approach constitutes a comprehensive, end-to-end simulation of the supernova evolution – from the first moments of ignition, through the weeks and months following the explosion – without resorting to any ad-hoc manipulation of model parameters. This methodology provides the most thorough means of evaluating the success and failures of the particular explosion paradigm, and offers important guidance for further development of the theory.

2. DFD Y12 EXPLOSION MODEL

The detonating failed deflagration (DFD) scenario of thermonuclear supernovae considers an off-center, mild ignition process in a degenerate Chandrasekhar mass carbon-oxygen white dwarf. In Paper I, we described detailed calculations of the explosion process as performed with the multi-physics hydrodynamics code FLASH (Fryxell et al. 2000). These calculations were all performed in two dimensions assuming axial symmetry. From the set of the models presented in that work, we have selected one example (Y12) for detailed analysis. Here we briefly review the salient features of the Y12 model from the point of view of the calculation of model observables.

In the Y12 model, the white dwarf is initially ignited within a small spherical region on the symmetry axis, 50 km in size and offset 12.5 km from the center. The resulting deflagration takes the form of a buoyantly rising, high temperature bubble filled with freshly synthesized nucleosynthetic products. This early phase is illustrated in Figure 1a, in which the bubble surface (identified with the edge of the deflagration front) is marked by the dark contour line.

As the rising bubble approaches the white dwarf surface, the outer layers of the star are deformed and laterally accelerated, leading to the production of a circular surface wave. By t=1.75 s (Figure 1b) that wave is seen to already have passed the stellar equator. By t=3.575 s (Figure 1c) the wave reconverges at the pole and begins radially compressing unprocessed stellar material. A jet-like flow develops in this confined region, radially expelling material from the system while at the same time forming a shock wave moving into the bulk of the star. The shock-wave is marked by the light blue line near $(r, z) \approx (0, -2.5 \times 10^8)$ cm in Figure 1c.

A short time later, the temperature in that shock-wave-dominated region exceeds the ignition temperature for the carbon/oxygen mixture, triggering a detonation through the shock-to-detonation mechanism (Paper I). Unlike in previous delayed-detonation models (e.g., Höflich et al. 1995; Gamezo et al. 2005), this transition to detonation is not inserted by hand but arises naturally in the course of the model evolution. Over the next 0.3 s, the detonation wave will progressively consume the bulk of the star (Figures 1d and 1e), and reprocess the material ejected in the initial deflagration phase. Burning ceases a few tenths of a second later. By $t = 5$ s (Figure 1f), the supernova shockwave has already completely swept through the portion of the star pre-expanded by the deflagrating bubble ($z > 0$), while it still remains trapped in the denser portion of the star ($z < 0$).

We followed the further evolution of the Y12 model up to $t = 100$ s after ignition. At this time, the ratio of internal to kinetic energy is found to be less than 1% at all points in the ejecta, indicating that the free expansion phase has been reached. We verified that the model velocity structure is homologous, that is, the local velocity is linearly related to the radius $\vec{v}(r, t) = \vec{r}(t)/t_0$ where $t_0 = 100$ s. Thus spatial coordinates can be transformed to velocity space using $\vec{v}(r, t) = 10^{-7}\ \vec{r}(t)$ km s^{-1}. The

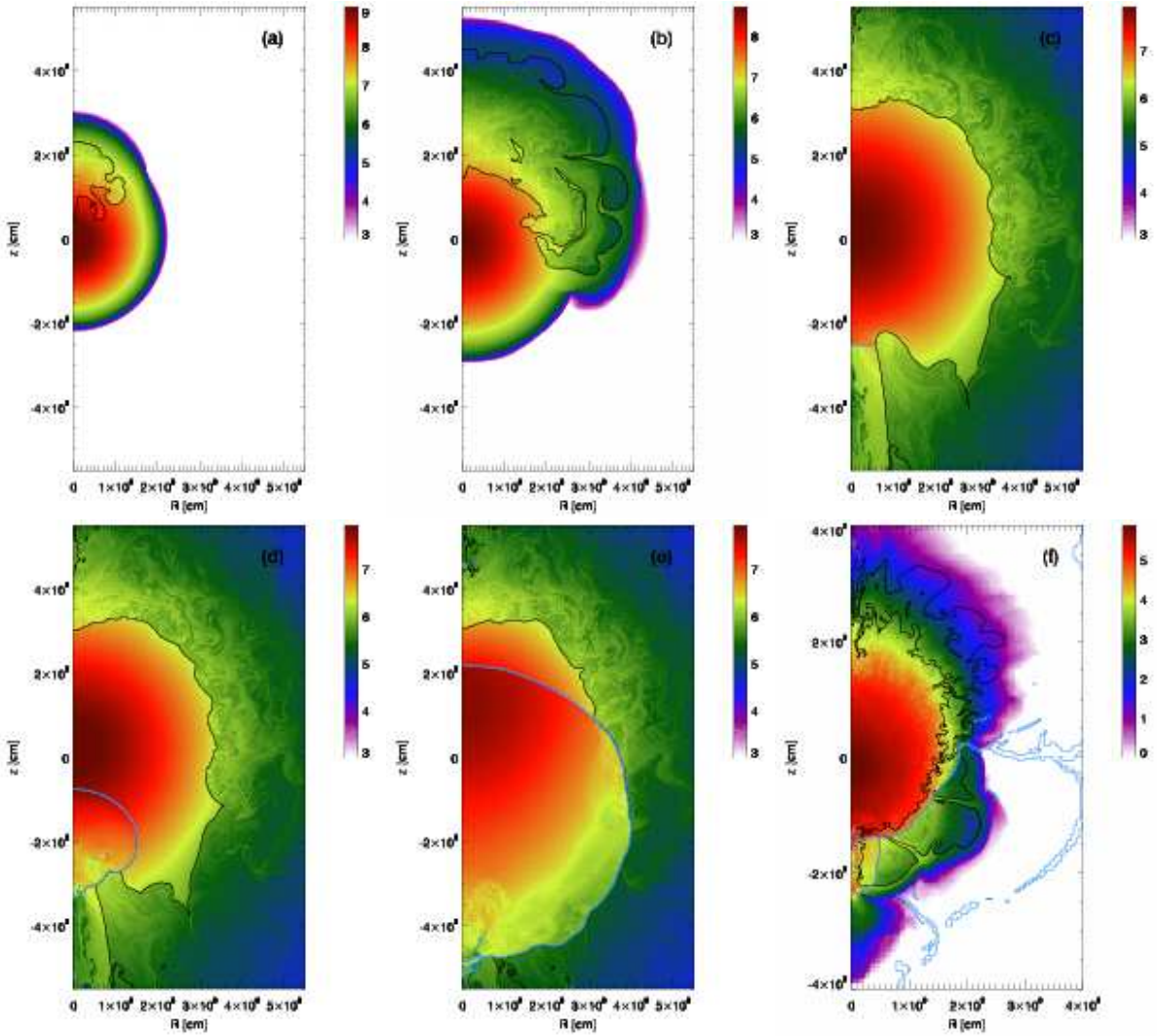

FIG. 1.— Y12 model of a thermonuclear supernova explosion. Shown is the temporal evolution of density in log scale at times $t = 1.25, 1.75, 3.575, 3.75, 4.0, 5.0$ s from panel (a) to (f) respectively (note the change of spatial scale between panel (f) and the rest of the sequence). The position of the deflagrating material is marked with black contours, while shockwaves are marked in light blue. The transition from deflagration to detonation is triggered by the shockwave visible in panel (c) at $(r, z) = (0, -2.5 \times 10^8)$. For more details, see the text.

total kinetic energy of the explosion is 1.36×10^{51} ergs and the total mass of ^{56}Ni produced is 0.93 $M_\odot$.

The density structure of the model at this final time (Figure 2) is nearly spherical, but with a slight "egg-shape", being more compact on one side. As seen in Figure 3, the characteristic ejection velocities are higher on the side from which the bubble emerged (the ignition side) and lower on the side from where the detonation took place (the detonation side). This is a result of the early expansion that occurred preferentially on the ignition side due to the passage of the deflagration bubble.

The compositional structure of the model, also illustrated in Figure 2, is well stratified on the large scale, and nearly spherical in shape. Interestingly, the entire compositional structure is offset by ~ 3000 km s^{-1} relative to the center of expansion. The innermost region of ejecta is rich in iron-group elements (specifically ^{56}Ni) and extends to $13,000$ km s^{-1} on the ignition side and 7000 km s^{-1} on the detonation side. Surrounding this is a shell rich in intermediate mass elements (IMEs), spanning the velocity range $7000 - 10,000$ km s^{-1} on the detonation side and $13,000 - 18,000$ km s^{-1} on the ignition side. Both ^{28}Si and ^{40}Ca are present in this IME shell, as marked respectively by the black and blue contour lines in Figure 2. Nearly the entire star is consumed by the explosion, with very little carbon/oxygen remaining.

We note that the detailed nucleosynthesis calculated in the Y12 model is only approximate (see Paper I). During the deflagration phase, nucleosynthesis was calculated using an approximate burner which tracked only the few most representative isotopes. The detonation phase employed a more extensive (but still approximate) 13-element network. Post-processing of the model using a more complete nuclear network is therefore necessary to more accurately specify the detailed model abundances. In particular, some fraction of the ^{56}Ni produced in the detonation phase may in fact represent stable iron group elements, while some fraction of the silicon group produced in the deflagration phase likely represents a distribution of various IMEs.

The inner layers of ejecta ($v \lesssim 15,000$ km s^{-1}) in

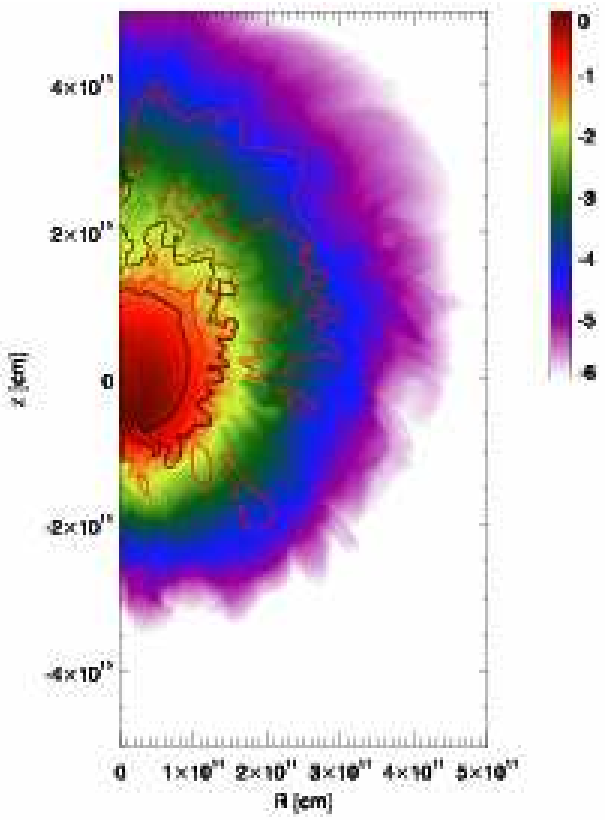

FIG. 2.— Final density structure of the Y12 DFD model of a thermonuclear supernova explosion in the homologous phase (t = 100 s). The density is shown in log scale. The spatial coordinates can be converted to velocity space using $\vec{v}(r,t) = 10^{-7}\vec{r}(t)$ km s^{-1}. The distributions of ^{28}Si and ^{40}Ca are shown in red and black contours, respectively. The contour levels correspond to $X(^{28}\mathrm{Si}) = 0.25$ and $X(^{40}\mathrm{Ca}) = 0.01$. The position of the inner IME-rich shell can roughly be identified with the distribution of ^{40}Ca. The material in the outer silicon-rich region was produced during the deflagration phase. The lack of calcium in the outer shell is the result of the simplified nuclear burning method used to calculate the deflagration. Note the relative smoothness of the inner shell compared to the inhomogeneity of the outer shell.

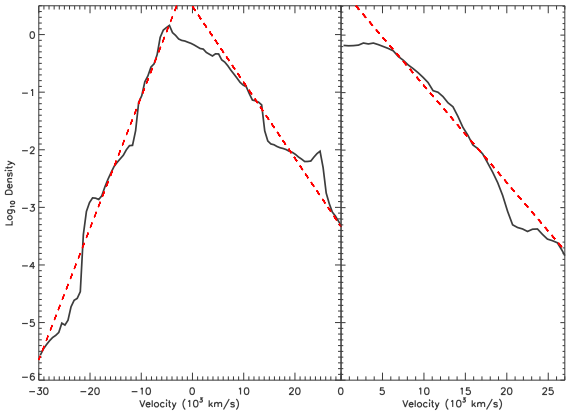

FIG. 3.— Density structure (solid lines, in log scale) of the Y12 DFD model in the homologous phase (t = 100 s) shown versus velocity coordinates. The dashed lines show the best fit exponential law $\rho(v) = \rho_0 \exp(-v/v_e)$. *Left:* Density along the z-axis (the symmetry axis) at $r = 0$. The ejecta is more extended for $z > 0$ (the ignition side) and characterized by an exponential velocity scale v_e = 3290 km s^{-1}. The ejecta is more compact for $z < 0$ (the detonation side) with v_e = 1900 km s^{-1}. The peak density is also slightly offset from the expansion center. *Right* Density along the r-axis at $z = 0$. The density law is characterized by v_e = 2575 km s^{-1}

the Y12 model are smooth and continuous, typical of the material processed solely by the detonation. This can be contrasted with the outermost layers of ejecta, which were perturbed initially by the surface wave created by the deflagration bubble. That turbulent-like flow involved mixing of the bubble material and unburned stellar matter, creating density and compositional inhomogeneities with a typical size of about ten degrees.

A characteristic feature of the model is the presence of two distinct shells rich in IMEs. The inner IME shell represents material synthesized by the detonation wave. The outer, high-velocity shell ($v \approx 25000-35000$ km s^{-1}) is composed chiefly of the material created and expelled during the deflagration phase. This high-velocity shell resembles the pancake structure described in the parameterized models of Kasen & Plewa (2005), except that in the Y12 model the material has a larger covering factor and a more irregular structure. Note that only silicon, and not calcium, is present in the high-velocity shell, an artifact of the approximate burner used during the deflagration phase. One expects that, had a more complete nuclear network been used, a significant amount of calcium would also be present. Rather than speculate as to that exact amount of calcium produced, we leave the compositional structure as is, referring the reader to the studies of Kasen & Plewa (2005).

Before considering the observable properties of the Y12 model, we mention a few limitations of the underlying explosion calculations. Although no tuning of the model parameters was required to obtain an explosion, the DFD mechanism itself is subject to uncertainties regarding the initial conditions, geometrical simplifications, and various numerical limitations. In Paper I, for example, a successful shock to detonation transition (SDT) was not achieved for all ignition configurations considered. This may indicate a lack of robustness of the underlying explosion mechanism, or may simply be a consequence of the relatively low numerical resolution of the calculations. A low resolution limits the size of the shocked regions, enhances numerical diffusion, and as a result may underestimate the actual post-shock temperatures and densities. These factors may artificially decrease the probability of SDT. On the other hand, numerical diffusion is a known source of mixing that may lead to artificial preheating and spurious ignition of fuel (Fryxell, Müller, & Arnett 1989). Although the transitions to detonation reported in Paper I are due to shock compression in nominally unburned material, the results are undoubtedly sensitive to possible contamination due to mixing, which may affect the likelihood of SDT. Even if a SDT is not achieved, it is still possible for a detonation to occur through the Zeldovich gradient mechanism (Khokhlov, Oran, & Wheeler 1997) once the deflagrating material perturbs and mixes with the surface layers of the star.

For completeness, we also summarize some more fundamental simplifications of the DFD explosion model. In particular, we took the progenitor to be a cold, static, non-rotating, unmagnetized, chemically homogeneous white dwarf. Although such a model is consid-

ered "standard" in most modern SN Ia explosion studies, theoretical work strongly suggests that most of these assumptions are in fact incorrect. The cores of massive white dwarfs are thought to be both convective and chemically stratified (Arnett 1969; Höflich & Stein 2002). Energy release from carbon burning likely occurs even before ignition, which may contribute to the pre-expansion of the progenitor and modify the energetics of the subsequent deflagration. Rotation of the white-dwarf can affect the structure of the convective core and may induce a large scale anisotropy of the explosion. Moreover, rotational shear may to some extent change the evolution of the deflagration front and further modify the effective flame energetics, which may influence the white dwarf pre-expansion. All of these elements necessarily contribute to the previously mentioned numerical uncertainties of the DFD explosion model, and deserve careful consideration in the future.

3. RADIATIVE TRANSFER CALCULATIONS

The observable properties of the Y12 DFD model have been calculated using the multi-dimensional time-dependent radiative transfer code `SEDONA` (Kasen et al. 2006). Given a homologously expanding SN ejecta structure, `SEDONA` calculates the full time series of emergent spectra at high wavelength resolution. Broadband light curves are then constructed by convolving the spectrum at each time with the appropriate filter transmission profile. `SEDONA` includes a detailed treatment of gamma-ray transfer to determine the instantaneous energy deposition rate from radioactive ^{56}Ni and ^{56}Co decay. Radiative heating and cooling rates are evaluated from Monte Carlo estimators, and the temperature structure of the ejecta determined by iterating the model to thermal equilibrium.

Several significant approximations are made in `SEDONA`, notably the assumption of local thermodynamic equilibrium (LTE) in computing the level populations. In addition, bound-bound line transitions are treated using the expansion opacity formalism (implying the Sobolev approximation) and an approximate two-level atom approach to wavelength redistribution. Special care was taken for the calcium lines, which were assumed to have pure scattering source functions for the reasons discussed in Kasen (2006). Note that `SEDONA` allows for a direct Monte Carlo treatment of line fluorescence, but due to computational constraints this functionality is not exploited here. See Kasen et al. (2006) for a detailed code description and verification, as well as tests of the expansion opacity and two-level atom approximations.

In the atmospheres of SNe Ia, the microscopic conditions assuring the establishment of LTE ionization and excitation are in fact not met. Nevertheless, a number of previous theoretical studies confirm the adequacy of LTE models in reproducing the qualitative spectral and photometric properties of SNe Ia (e.g., Höflich et al. 1995; Baron et al. 1996; Pinto & Eastman 2001). The LTE simplification can be expected to result in quantitative errors in the model light curves, especially at later times (~ 60 days after explosion) when non-LTE ionization effects become increasingly significant. In addition, the model predictions in this paper are subject to the further inadequacies of the two-level atom framework and the available atomic line data (Kasen et al. 2006; Kasen 2006). We hope to reduce these uncertainties in future work by relaxing some of the simplifying assumptions underlying the radiative transfer calculations.

The time-dependent light curve calculations in this paper were computed using the following numerical resolution: *Spatial:* A 100×50 cylindrical grid extending to a maximum velocity of 30,000 km s^{-1} and with a cell length of 600 km s^{-1}; *Temporal:* 100 time points spanning the epochs day 2 to day 80 with logarithmic spacing $\Delta \log t = 0.175$; *Wavelength:* Spanning the range 100-25000 Å with constant resolution of 100 Å. Extensive testing confirms the adequacy of this resolution for the problem at hand. A total of 10^9 photon packets were used in the Monte Carlo procedure. The emergent light curves and spectra were generated by collecting escaping packets into 50 separate viewing angle bins.

The time-dependent `SEDONA` light curve calculation provides the full spectral time series of the model, however to further improve our synthetic spectrum results we performed further time-independent calculations at five select epochs using both higher resolution (200×100 spatial grid, 5 Å wavelength resolution) and a large number (10^8) of packets. The emergent bolometric luminosity parameter for these static calculations was determined from the full light curve calculation. The static synthetic spectra achieve higher signal-to-noise, but otherwise show excellent agreement with the time-dependent spectra, except in small-scale features of size < 100 Å. In addition, one static spectrum near maximum light ($t_{\rm exp}$= 18 days) was run using 10^{12} packets in order to study the $\lesssim 1\%$ polarization levels.

4. COMPARISON TO OBSERVATIONS

We present below the synthetic optical/near-infrared light curves, spectral time series, and spectropolarization of the Y12 model, comparing and contrasting the results with observations of representative SNe Ia. The properties of observed SNe Ia vary somewhat from object to object. We make no attempt here to find an optimal correspondence with the Y12 model, rather we simply compare to the more well-known, well-studied objects.

4.1. *Light Curves and Color Evolution*

In Figure 4, we show the synthetic $UBVRIJHK$ light curves of the Y12 model as compared to SN 2001el, a well observed and photometrically normal SNe Ia (Krisciunas et al. 2003). There is some uncertainty in the total dust extinction to SN 2001el, which is estimated between $A_v = 0.35 - 0.77$ depending on the method used. Here we adopt the values $A_v = 0.57$ and $R_v = 2.88$ (Krisciunas et al. 2003; Wang et al. 2003) and correct for extinction using the dust laws of Cardelli et al. (1989).

Given the intrinsic asymmetry of the Y12 model, we consider for now only the equatorial view ($\theta = 90°$) of the ejecta, deferring discussion of the orientation effects to §5. From this angle, the model light curves reach a peak absolute magnitude of -19.57 in B, and -19.61 in V. In Figure 4 we have adopted a distance modulus to SN 2001el of 31.65 mag so as to align the observed peak magnitudes with those of the model. Krisciunas et al. (2003) deduce a significantly lower distance of 31.29 ± 0.08 mag on the basis of the supernova photometry. This suggests that the Y12 model is

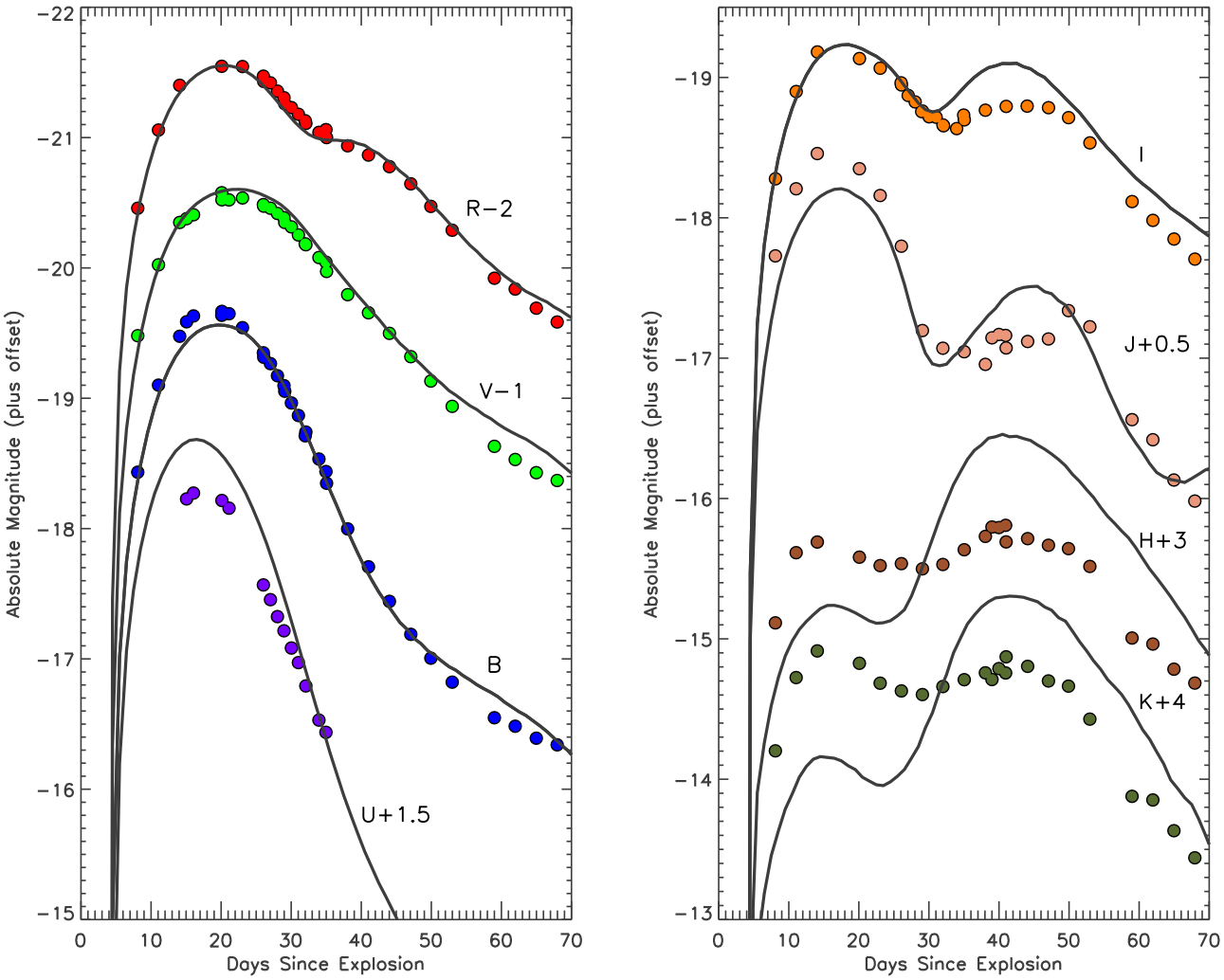

FIG. 4.— Synthetic $UBVRIJHK$ light curves of the Y12 DFD model as seen from an equatorial view ($\theta = 90°$, solid lines) compared to observations of SN 2001el (filled circles, Krisciunas et al. 2003). To align the models and observations, we adopt a distance modulus for SN 2001el of $\mu = 31.65$, which is 0.35 mag greater than the best estimate.

~ 0.35 mag too bright compared to SN 2001el – not surprising given the explosion produced over 0.9 $M_\odot$ of ^{56}Ni. This discrepancy may be mitigated somewhat if detailed nucleosynthesis calculations reveal that some fraction of the ^{56}Ni in the Y12 model in fact corresponds to stable iron group elements. Note also that the DFD scenario encompasses a family of explosion models which produce greater or lesser amounts of ^{56}Ni, depending on the initial ignition conditions (Paper I).

The shape of the model optical light curves match qualitatively those of SN 2001el, especially in the B-, V- and R-bands. The rise time to B-band maximum is 18.8 days for the model, similar to that observed among typical SNe Ia (Riess et al. 1999a; Conley et al. 2006). The subsequent decline from peak is also quite consistent with the observations of SN 2001el and other typical SNe Ia, with a drop in B-band magnitude 15 days after peak of $\Delta m_{15}(B) = 1.19$ mag. However, given that brighter SNe Ia generally display broader light curves, this decline rate may be considered too fast in light of the high peak magnitude of the model. As we discuss in §5, the decline rates of the model light curves in fact depend rather sensitively on the orientation.

A distinct secondary maximum in the model I- and J-band light curves occurs about three weeks after B-maximum. A much weaker secondary maximum is also present in the R-band. The same double-peaked morphology is seen in the SN 2001el observations, although the size and timing of the secondary maximum differ somewhat from the model. The properties of the secondary maximum in fact vary substantially from supernova to supernova (Nobili et al. 2005), and also depend sensitively on the model parameters (Kasen 2006). Brighter SNe Ia (i.e., those with larger masses of ^{56}Ni) typically display more prominent secondary maxima. The overly bright I-band secondary maximum of the Y12 synthetic light curve indicates, in part, its overly large mass of ^{56}Ni compared to SN 2001el.

The model H- and K-band light curves show a much poorer correspondence with the observations, with the secondary maximum being much too bright relative to the first one. As discussed by Kasen (2006), this sort of discrepancy is attributable, in large part, to the inadequacy of the atomic line data used in the transfer calcula-

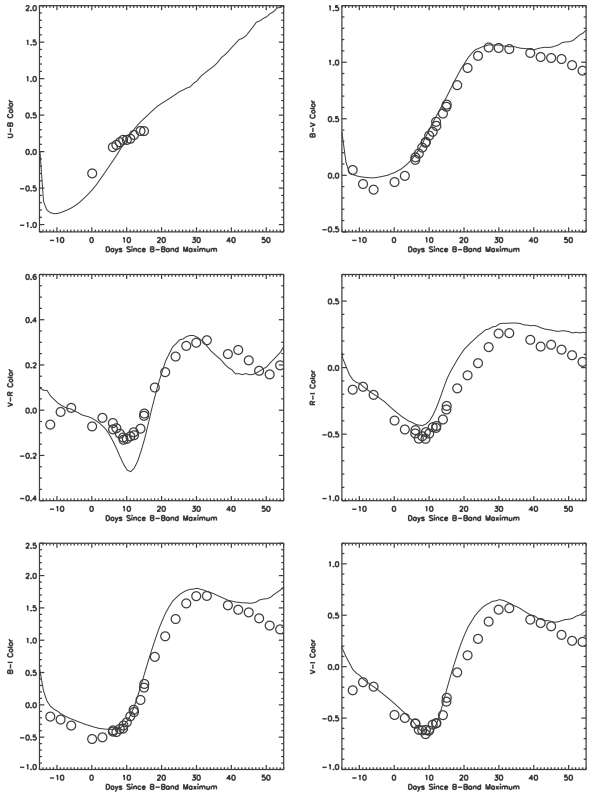

FIG. 5.— Temporal evolution of the colors of the Y12 DFD model as seen from an equatorial view ($\theta = 90°$, solid lines) compared to observations of SN 2001el (open circles, Krisciunas et al. 2003).

tions. The Y12 model, however, shows a relatively poorer match to SN 2001el when compared to other models considered in Kasen (2006), likely due again to the relatively large ^{56}Ni mass.

The optical color curves of the model are compared to those of SN 2001el in Figure 5. In general, the curves show qualitative agreement up to about 40 days after B-band maximum. At later times, the model's color get progressively redder, while the observations show the opposite trend. It is at these late epochs, when LTE predicts neutrality in the ejecta, that non-thermal ionization by the products of radioactive decay becomes significant (Swartz 1991). Thus our transfer calculations should be considered less reliable at these phases.

4.2. *Spectral Evolution*

The spectra of SNe Ia consist of broad P Cygni features superimposed on pseudo-blackbody continuum. By identifying individual absorption features and measuring their Doppler-shifts, we probe the composition and velocity of the absorbing ejecta material. As the SN material expands and geometrically dilutes, the photosphere recedes, revealing emission from progressively deeper layers. The spectral time-series thus provides a scan of the multi-layered ejecta compositional structure.

We choose to compare the synthetic spectra of the Y12 DFD model to observations of SN 1994D, a well-sampled SN Ia with normal spectral characteristics (Patat et al. 1996; Meikle et al. 1996). The dust extinction of SN 1994D is believed to be very small, and we make no corrections for reddening. Branch et al. (2005)

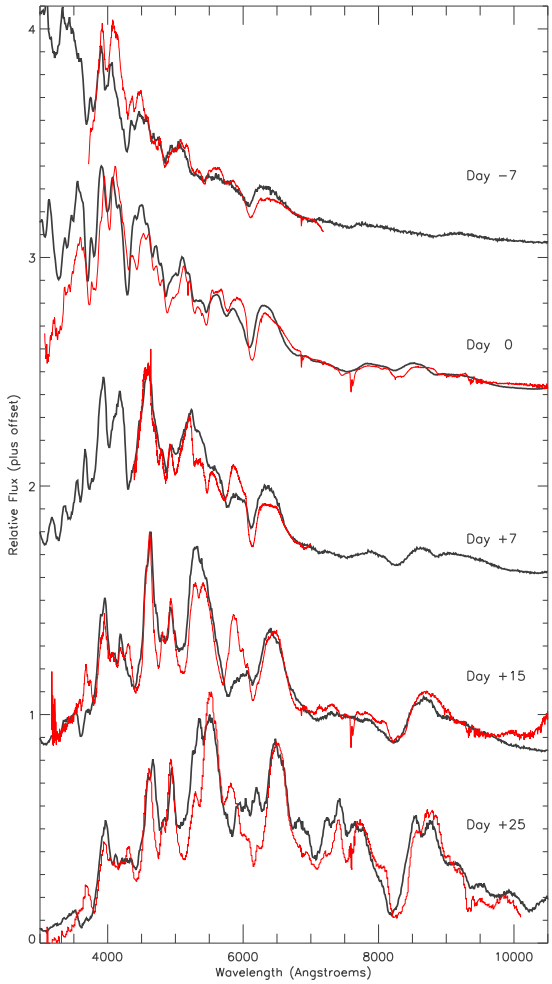

FIG. 6.— Synthetic spectra at five different epochs of the Y12 DFD model as seen from an equatorial view ($\theta = 90°$, black lines) compared to those of SN 1994D (red lines, Patat et al. 1996; Meikle et al. 1996). Labels give the day relative to B-band maximum.

provide a comprehensive line identification and spectroscopic analysis of SN 1994D. In addition, SN 1994D has been used to validate several other 1-dimensional explosion models such as W7 (Lentz et al. 2001) and various delayed-detonation models (Höflich 1995; Baron et al. 2006), allowing cross-comparison of the Y12 model with other theoretical calculations.

In Figure 6, we show the synthetic spectra of the Y12 model (as seen from an equatorial view) at several different epochs – viz., day $-7, 0, +7, +15$, and $+25$ days with respect to B-band maximum. In general, we find the synthetic spectra to be in impressively good agreement with those of SN 1994D. The quality of fit is comparable to (and often better than) that obtained with classic 1-dimensional models, such as W7 and the delayed-detonation models.

At maximum light ($t_{\rm exp} = 18.8$ days), the model reproduces all of the major spectral features identified in the observations. These are primarily lines from IMEs, in particular three Si II absorption features (near 4000 Å, 5850 Å, and 6150 Å), the S II "W"-feature (near 5200 Å), and the Ca II H&K and IR-triplet features (near 3600 Å

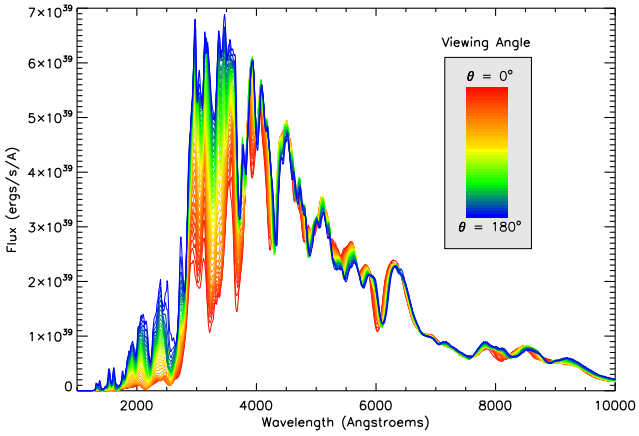

FIG. 7.— Variation with viewing angle of the Y12 DFD model synthetic spectrum at maximum light ($t_{\rm exp}$= 18 days). The angle $\theta = 0°$ corresponds to the view from the ignition side ($z > 0$ in Figure 2).

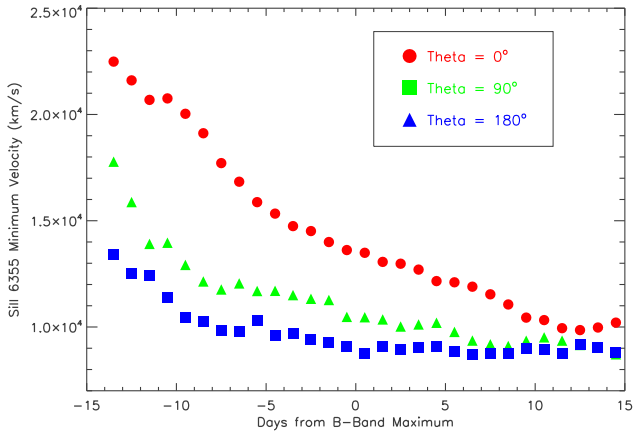

FIG. 8.— Temporal evolution of the Si II 6150 absorption minimum velocity as seen from three different viewing angles. The angle $\theta = 0°$ corresponds to the view from the ignition side ($z > 0$ in Figure 2). while $\theta = 90°$ corresponds to an equatorial view and $\theta = 180°$ corresponds to the view from the detonation side ($z < 0$). The variation in the model velocity evolution can be compared the observed diversity in SNe Ia (Benetti et al. 2005, Figure 1).

and 8200 Å, respectively). The only feature not well fit at maximum light is the double absorption near 4600 Å, due to blends of Mg II and Si III. Interestingly, this feature is peculiar in SN 1994D, and most other normal SNe Ia more closely resemble the model (e.g., SN 1981B, Branch et al. 1985).

The blueshifts of the absorption minima in the maximum light spectrum indicate that the model velocities are in broad agreement with the observations. In detail, however, the model absorptions are systematically bluer than the observations, most conspicuously in the Si II 6150 and Ca II IR triplet lines. We note that the blueshift of the model absorption changes with orientation (see §5) and also is observed to vary from supernova to supernova (Benetti et al. 2005). The velocity differences noted in Figure 6 are therefore within the observed scatter of normal SNe Ia.

A week after maximum light ($t_{\rm exp}$ = 25 days), most of the same IME features are still present in the observed spectra, while a prominent Na I feature emerges at 5600 Å, blending with the smaller of the Si II features. The approximate alpha network used in the explosion model did not include sodium, therefore the synthetic spectrum does not reproduce the sodium feature. This issue will be addressed in future models by including more detailed nucleosynthesis. Among the other features, we note that the sulfur W-feature, well fit by the model at maximum light, appears too weak at this epoch.

At later times, the SN photosphere recedes into the metal core of ejecta, and the spectra progressively become dominated by lines from iron group elements. The model spectra at 14 and 21 days after B-maximum well account for the observed features, with the exception of the Na I line.

5. INTRINSIC MODEL ASYMMETRY AND DIVERSITY

A major advance offered by our multi-dimensional radiative transfer calculations is the ability to study the dependence of the model observables on the viewing angle. In the DFD model, the fundamental orientation effects arise from the variation of the characteristic ejecta expansion velocities along different directions. As discussed in §2 (see also Paper I) this distortion reflects the inherent asymmetry of the initial conditions and subsequent deflagration. The global asymmetry of the partially burned white dwarf is then imprinted on the dynamical and compositional structure of the ejecta by the off-center detonation.

5.1. *Photometric and Spectroscopic Diversity*

The asymmetry in the Y12 ejecta structure leads to two significant orientation effects in the model spectrum, both clearly visible in the maximum-light spectrum shown in Figure 7.

First, the blueshift of most spectral absorption features depends on the viewing angle, becoming larger as one looks closer to the ignition side. This is due to the generally higher expansion velocities of the IME shell on that side of the ejecta. Figure 8 quantifies this Doppler shift dependence by plotting the time evolution of the velocity of the prominent Si II absorption near 6150 Å, as seen from several viewing angles. In this figure we have measured the velocity directly from the Doppler shift of the Si II absorption minimum for each of the synthetic spectra in our daily spectral time-series. Such a method corresponds exactly to what is done in the observational studies. By contrast, most other time-dependent SN radiative transfer calculations determine only the velocity of the SN photosphere, which may or may not coincide with that of the Si II line.

Near maximum light, the Si II velocity varies from $9,000$ to $13,500$ km s^{-1}, or by nearly 40%, depending on the viewing angle. The velocity is largest and has the fastest rate of decrease with time when observed near the ignition side ($\theta = 0°$). For viewing angles away from the ignition side, the velocity of the Si II feature is lower and almost constant with time. This variety of velocity gradients can be compared to Figure 1 of Benetti et al. (2005), which demonstrates a strikingly similar diversity among observed SNe Ia. The Y12 model prediction is therefore, at first glance, in reasonable agreement with the statistical behavior of the observational sample. On the other hand, the cluster analysis of Benetti et al. (2005)

suggests that observed SNe Ia can be divided into two distinct classes of "high" and "low" velocity gradient. In the Y12 model, by contrast, the orientation effect leads to a range of events intermediate the two classes. This continuous behavior appears, at first glance, inconsistent with the dichotomy of Benetti et al. (2005), although a detailed statistical comparison would be needed to truly confirm the discrepancy.

The second consequence of the model asymmetry on the maximum light spectrum is that the flux level at shorter wavelength shows a strong variation with viewing angle. In the B-band (4000 Å $\lesssim \lambda \lesssim$ 5000 Å) this variation is only of order 10%, however it increases to a factor of ~ 4 in the U-band (3200 Å $\lesssim \lambda \lesssim$ 4000 Å) and is even larger in the ultraviolet. The effect is a result of the aspherical distribution of iron group elements in the ejecta. On the ignition side ($\theta = 0°$) iron group species extend to a velocity $v \approx 13,000$ km s^{-1}, whereas on the detonation side ($\theta = 180°$) these elements are restricted to velocities $v \lesssim 7,000$ km s^{-1}. It is primarily the line blanketing from iron group lines that determines the flux level at shorter wavelengths. When viewed at $\theta = 180°$, the relative lack of iron group elements at higher velocities leads to significant reduction in the degree of line blanketing, and hence a spectrum that is brighter at bluer wavelengths.

At two weeks after maximum light, the same sort of orientation effects are visible in the synthetic spectra (Figure 9). By this epoch, the layers of ejecta rich in iron-group elements have begun to recombine from doubly to singly ionized, and features from Fe II/Co II lines dominate the spectrum. Again, because of the aspherical distribution of iron group elements, the flux level at shorter wavelengths shows a strong dependence on the viewing angle. However, at this time the asymmetry affects wavelengths even longer than at maximum light, as Fe II/Co II lines have become prominent in the optical part of the spectrum. The B-band portion of the spectrum now shows flux variations by a factor of nearly two. This line-blanketing effect leads to a strong dependence of the model $B-V$ color evolution on orientation, especially after maximum light, as seen in Figure 10.

Clearly this orientation effect has important implications for the B-band light curves of the model, and consequently the SN Ia width-luminosity relationship. The development of Fe II/Co II line blanketing largely determines the B-band decline rate $\Delta m_{15}(B)$ of SNe Ia (Kasen & Woosley 2006). As seen in Figure 11, the aspherical distribution of iron group elements in the Y12 model thus leads to significant variations in $\Delta m_{15}(B)$ with viewing angle. The decline rate changes from $\Delta m_{15}(B)$= 0.96 mag at $\theta = 0°$ to $\Delta m_{15}(B)$= 1.36 mag at $\theta = 180°$. This is a good fraction of the total range of decline rates noted in the observational sample of SNe Ia.

The peak B-band magnitude of the Y12 model also varies with viewing angle, although to a lesser extent, from $M_B = -19.43$ mag at $\theta = 0°$ to $M_B = -19.56$ mag from the opposite side. The correlation between $\Delta m_{15}(B)$ and M_B thus has the same sign as the observed width-luminosity relation, in that broader SNe are generally brighter. However, as seen in Figure 11 (right panel), the correlation is too weak as compared to the observed relation of Phillips et al. (1999). Thus

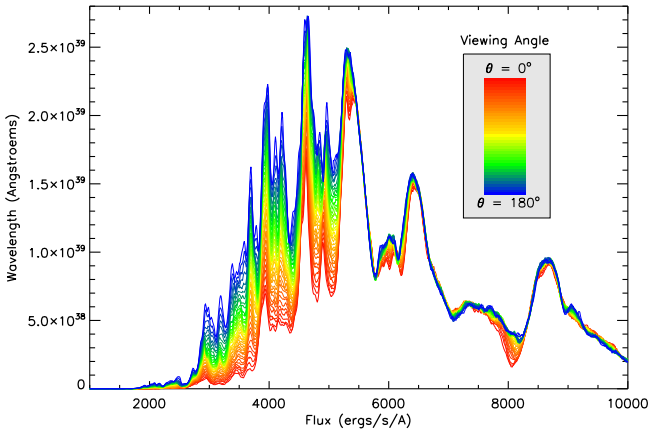

FIG. 9.— Variation with viewing angle of the Y12 DFD model synthetic spectrum two weeks past maximum light ($t_{\rm exp}$= 32 days). The angle $\theta = 0°$ corresponds to the view from the ignition side ($z > 0$ in Figure 2) Note that the strong flux variation has shifted redward when compared to that at maximum light (Figure 7).

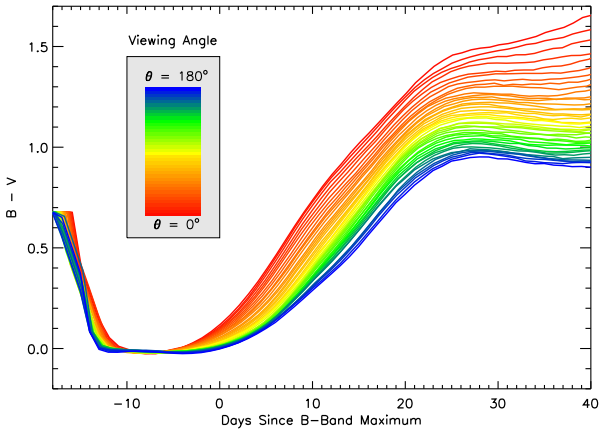

FIG. 10.— Variation with viewing angle of the Y12 DFD model synthetic $B-V$ color with time. The angle $\theta = 0°$ corresponds to the view from the ignition side ($z > 0$ in Figure 2).

the asymmetry of the Y12 model could at most be considered as a potential source of dispersion in the width-luminosity relation. The model intrinsic dispersion is $\sigma \approx 0.13$ mag, roughly equal to the level noted in observations (Hamuy et al. 1996) and leaving little room for a contribution from observational or other errors.

As also seen in Figure 11 (right panel), the light curves of the Y12 model appear to be systematically brighter than the observations, given their range of $\Delta m_{15}(B)$. The shaded band in the figure is the width-luminosity relation of Phillips et al. (1999) with an assumed calibration of $M_B = -19.3$ mag for $\Delta m_{15}(B) = 1.1$ mag and with a dispersion $\sigma = 0.15$ mag. The model points lie roughly 0.25 mag above this relation. The significance of this discrepancy is debatable, as the absolute calibration of the empirical width-luminosity relation is subject to uncertainties in the distances to SNe Ia, while the model light curves may possess systematic errors of order 0.1-0.2 mag due to approximations made in the radiative transfer calculations.

The variation in the B-band magnitude with viewing

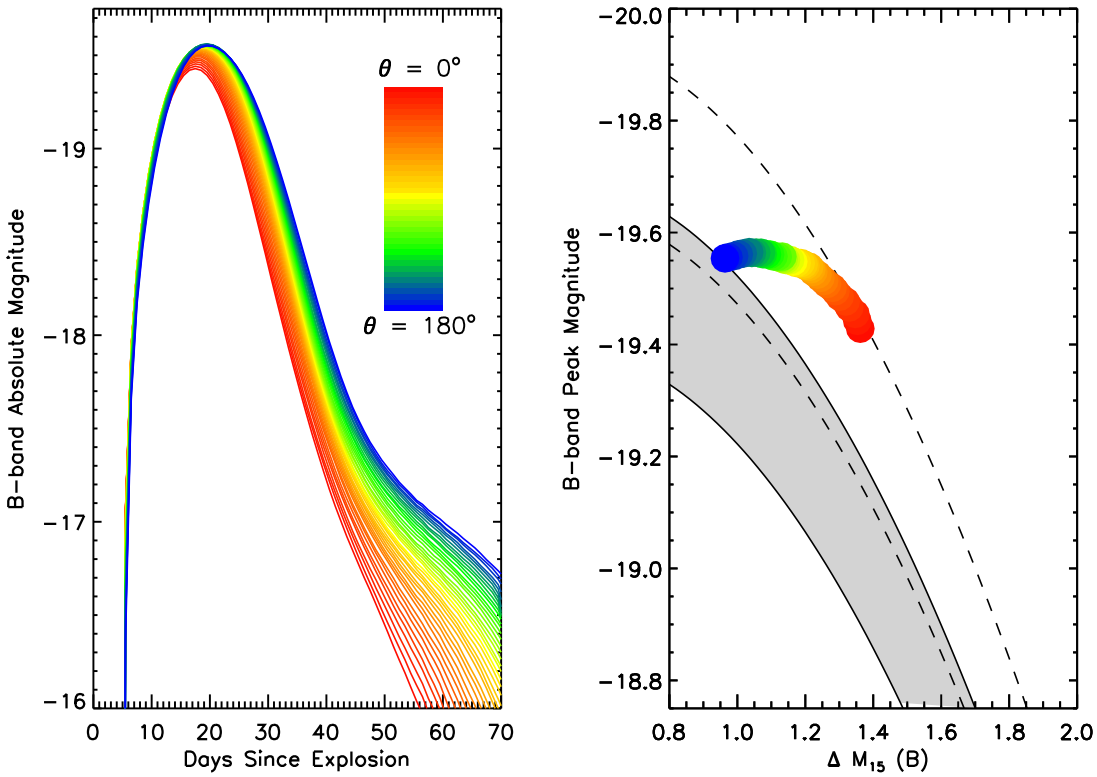

FIG. 11.— *Left:* Variation of the Y12 model B-band light curve with viewing angle. $\theta = 0$ corresponds to the view from the ignition side ($z > 0$ in Figure 2). *Right:* Relationship between the model peak B-band magnitude M_B and decline rate $\Delta m_{15}(B)$ as seen from different viewing angles. Color coding is the same as in the left panel. The shaded region is the observed relation of Phillips et al. (1999) with a calibration $M_B = -19.3$ mag at $\Delta m_{15}(B) = 1.1$ mag and spread of $\sigma = 0.15$ mag. The dotted lines show the same relationship shifted upward by 0.25 mag.

angle becomes even more dramatic at later times, and exceeds 1.5 mag at 40 days after B-maximum. This is larger than the ~ 1 mag dispersion seen in the observational sample (Riess et al. 1999b). Note, however, that the increased uncertainties in the radiative transfer at later times (as noted in §4.1) may contribute to the extreme spread in model B-magnitudes at these epochs.

5.2. *Polarization*

Polarization measurements provide the most direct probe of the asphericity of the SN ejecta. Light is polarized by electron scattering in the hot, ionized SN envelope. Detection of a finite net polarization indicates a preferred direction in the scaterring medium, and hence a departure from spherical symmetry. Spectropolarimetry is a challenging endeavor, as the light from SNe is dim and quickly fading, and the observed polarization levels are typically small, $P \lesssim 1\%$. Nevertheless, intrinsic polarization has now been clearly detected in several SNe Ia, both in the lines and the continuum (Howell et al. 2001; Wang et al. 2003; Leonard et al. 2005; Chornock et al. 2006). The sample size of objects with high signal-to-noise spectropolarimetry is unfortunately still rather small, and the observations are also subject to uncertainties in the degree of interstellar polarization caused by scattering by dust grains along the line of sight.

The continuum polarization level (i.e., the degree of polarization at wavelengths where electron scattering is the dominate opacity) provides the most basic measure of global asymmetry in the bulk SN ejecta. For the Y12 model, the continuum polarization is in fact very small during the epochs around and after maximum light. This reflects the fact that the density contours of the ejecta are not grossly aspherical. Moreover, the primary mode of the model's "egg-shaped" density structure is on a 180° scale, whereas the continuum polarization measures differences oriented 90° apart. In particular, while the polarization of light scattered from the ignition side of the ejecta is enhanced compared to a spherical model, this is nearly counter-balanced by the relative decrease in the polarization of light scattered from the compact detonation side 180° away. The polarized flux from the polar regions of the Y12 model then nearly equals the orthogonally oriented polarized flux from the equatorial regions. We therefore find that at maximum light, the continuum polarization of the Y12 model is small, $P < 0.1\%$, from all viewing angles. This is smaller than the continuum polarization of $P \approx 0.3\%$ typically observed in SNe Ia (e.g., SN 2001el, Wang et al. 2003). Given the signal-to-noise of most spectropolarimetry observations, a polarization of $P < 0.1\%$ is usually indistinguishable from zero.

Although the continuum polarization of the Y12 model is small at maximum light, the polarization over line features can be substantial. In Figure 12 we show the synthetic model polarization spectrum at maximum light, as seen from several viewing angles. Although nearly 10^{12}

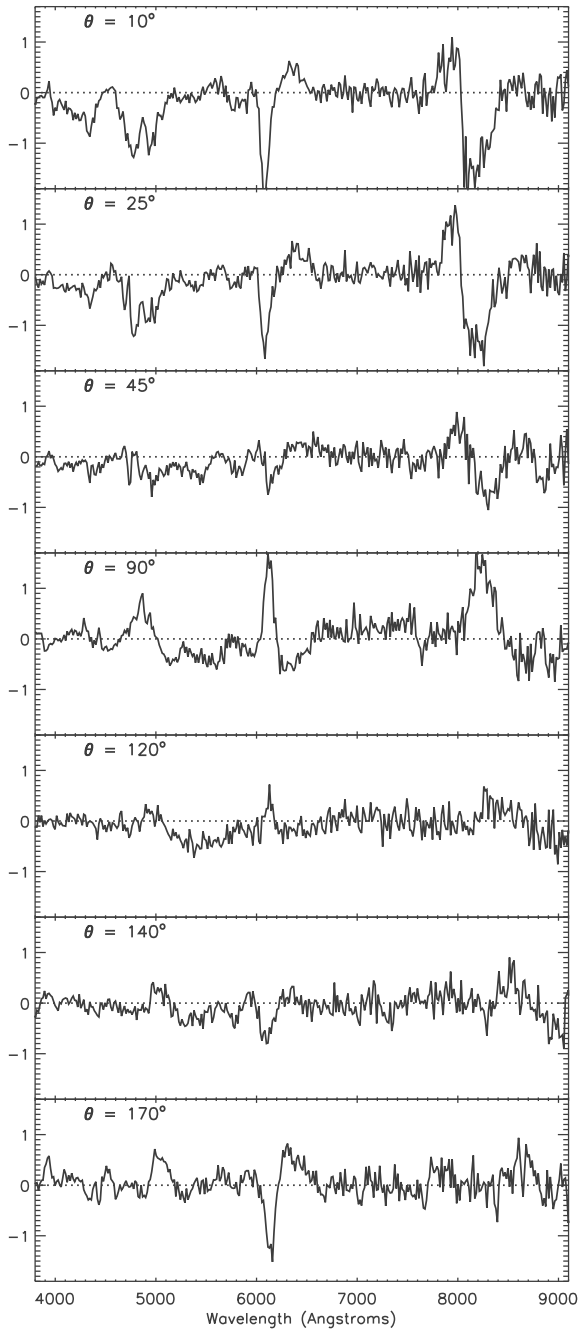

FIG. 12.— Synthetic polarization spectrum of the Y12 DFD model near maximum light ($t_{\rm exp}$= 18 days) as seen from several viewing angles θ. Small scale fluctuations represent the level of Monte Carlo noise in the calculation.

photon packets were used in this Monte Carlo calculation, the synthetic polarization spectra still show random noise at a level $\sim$ 0.1%. Nevertheless, the broad line features are easily discernible among the high-frequency fluctuations. The most prominent polarization features are due to the Si II absorption feature near 6150 Å, the

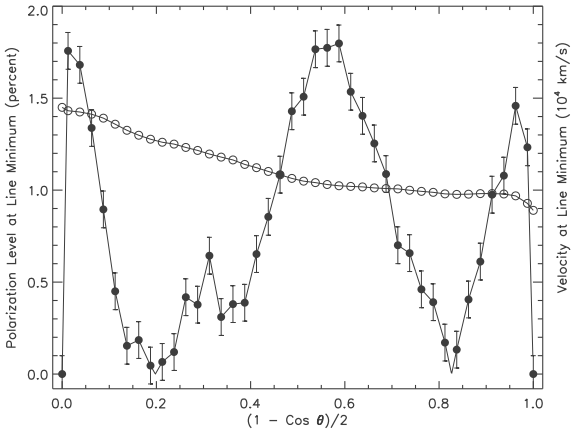

FIG. 13.— Velocity (open circles, in 10^4 km s^{-1}) and absolute value of the polarization (closed circles, in percent) measured at the line minimum of the Si II 6150 feature of the Y12 model at maximum light. The size of the error bars (0.1%) roughly represents the level of Monte Carlo noise in the polarization calculations. The abscissa is $x = (1-\cos\theta)/2$ where θ is the viewing angle. The probability of observing the model within the range $x = (x_1, x_2)$ is then easily figured as $p = x_2 - x_1$. The polarization cancels by symmetry at $\theta = 0°$ and 180° and so has been set to zero at these points.

Ca II IR triplet near 8200 Å, and the blend of Fe II lines near 4900 Å. The polarization over the Si II absorption feature reaches nearly 2% from certain viewing angles.

The line polarization of the Y12 model reflects the global asymmetry of the ejecta compositional structure, which results in an asymmetrical distribution of the line opacity. From certain viewing angles, the opacity from a strong line partially eclipses the underlying electron scattering photosphere, leading to an incomplete cancellation of the polarization over the wavelengths of the line absorption feature (Kasen et al. 2003). In the Y12 model, the most important asymmetry is that the distribution of IME-rich material extends to a higher velocity on the ignition side of the ejecta. In some respects, this asymmetry resembles that of the "pancake" geometry studied in Kasen & Plewa (2005). although in the present case the excess of IME-rich material abuts the primary IME shell, rather than being detached from it. The dependence of the line polarization on viewing angle thus resembles that explained in Kasen & Plewa (2005) – in particular, the line polarization is negative for small viewing angles ($\theta \lesssim 45°$) but flips sign for intermediate viewing angles ($\theta \approx 90°$).

Although we have no direct way to determine the viewing angle itself from SN observations, what we can study is the correlations between different angle dependent observables. In particular, it is useful to study the relation between the velocity of a line and its polarization, where both quantities are measured at the minimum of the flux absorption feature. In Figure 13, we plot these values for the Si II 6150 feature of the Y12 model, as derived from the maximum light polarization spectrum. In the figure, we chose the abscissa to be $x = (1 - \cos\theta)/2$, where θ is the viewing angle. The probability of observing the model within the range $x = (x_1, x_2)$ is then simply given by $p = x_2 - x_1$.

As discussed already (§5.1), for viewing angles towards the ignition side ($x \lesssim 0.1$ or $\theta \lesssim 35°$) the Si II velocity is

unusually high ($v \approx 14,000$ km s^{-1}). From these angles the Si II polarization is also always large ($P \sim 1-2\%$). A similar trend appears in the observations. Among the limited number of SNe Ia with spectropolarimetry, the Si II polarization is found to be largest in the two objects with the highest Si II absorption velocities (SN 2002bf and SN 2004dt, Leonard et al. 2005). The Y12 model predicts such events should be observed roughly 10% of the time.

From viewing angles away from the ignition side, the Si II polarization of the Y12 model may be either small or large. For $45^\circ \gtrsim \theta \gtrsim 78^\circ$ ($x = 0.15 - 0.4$), the model generally reproduces the low polarization levels and moderate line velocities characteristic of typical events like SN 2001el (Wang et al. 2003) and SN 2003du (Leonard et al. 2005). However, the Y12 model also predicts that some SNe Ia should exhibit high Si II polarization accompanied by low or moderate Si II line velocity. In particular, for $x = (0.45, 0.70)$ and $x = (0.9, 1.0)$ the polarization is $P \lesssim 1.0\%$ while the velocity is only $v \approx 9,000 - 10,000$ km s^{-1}. According to the model, such objects should be observed roughly 35% of the time, however no SN Ia with this characteristic has yet been found.

On the whole, the Y12 model predicts that the Si II line polarization will be greater than 1% from almost half of all possible viewing angles, which is generally higher than the average level of line polarization noted in the current (albeit limited) observational sample of SNe Ia. This suggests that the degree of compositional asymmetry in the model ejecta structure may be too extreme. This same conclusion had already been indicated by the large dispersion in the B-band decline rates (§5.1).

In addition to a global asymmetry, the IME layer of the Y12 model possesses numerous compositional inhomogeneities ("clumps") of typical size ten degrees. These were the result of the original turbulent-like flow of the deflagration material across the white dwarf surface. The signatures of these clumps, however, are not readily discernible in the polarization spectra of Figure 12. In this 2D calculation, the global asymmetry of the IME distribution dominates the polarization signal. In a fully 3D calculation, on the other hand, the IME clumps would lead to some deviation of the line polarization from a single axis of symmetry. This spectropolarimetric signature has been used to infer clumpiness in the IME layers of some observed SNe Ia (Wang et al. 2004). In this sense, the DFD scenario is notable in its ability to produce a clumpy outer layer of IME while retaining a rather smooth distribution in the inner ejecta.

The Y12 model also possesses clumps of IME at very high velocity ($v = 25,000 - 35,000$ km s^{-1}) representing material produced and expelled during the deflagration phase. Assuming these clumps were to possess a moderate abundance of calcium, one would expect to observe high velocity, highly polarized Ca II IR triplet absorption features in the maximum-light spectrum, similar to those discussed in Kasen & Plewa (2005). However, because the approximate nucleosynthesis employed during the deflagration phase of the explosion calculation did not include calcium, the high-velocity material does not in fact influence our current synthetic flux or polarization spectra. Given the low densities in these layers, the lines from all other elements besides calcium are too weak to be seen.

More detailed and conclusive studies of the ejecta geometry of SNe Ia will be possible once the database of spectropolarimetry observations is expanded, such that for each subclass of SNe Ia we have enough events to sample all viewing angles in a uniform way (e.g., always at exactly the same epoch). Figure 13 is just one demonstration of how we can use such a data set to powerfully constrain multi-dimensional models of SNe Ia.

6. SUMMARY AND CONCLUSIONS

We presented the model observable properties of one example of the DFD explosion scenario of thermonuclear supernovae. The explosion model involved the off-center ignition of Chandrasekhar-mass white dwarf which later underwent a transition from deflagration to detonation and produced an energetic explosion. The model was expanded well into the homologous phase, and then used as input to time-dependent multi-dimensional radiative transfer calculations. The transfer calculations supplied the emergent broadband light curves, color evolution, spectral time-series, and polarization of the model, all of which were critically evaluated against examples of well-observed, standard SNe Ia.

The calculations presented here were intended primarily to develop and apply a methodology of validating multi-dimensional SN models against observations. They represent the first extensive comparison of a self-consistent multi-dimensional SN Ia model against observations, and comprise one of the most comprehensive evaluations of any SN model to date. On the whole, the properties of the Y12 DFD model appear fairly consistent with observations, although certain discrepancies are also apparent. We summarize the primary successes and failures of the model as follows:

- The shape of the model broadband light curves resembles observations of the normal Type Ia SN 2001el. However, given the model's large ^{56}Ni mass (0.93 $M_\odot$), the synthetic light curves are generally brighter than the typical SNe Ia, by about 0.35 mag. The model light curves reach a peak absolute magnitude of -19.57 in B, and -19.61 in V, as viewed from the equatorial direction ($\theta = 90^\circ$).

- The B-band decline rate of the model ($\Delta m_{15}(B) = 1.19$ mag, as viewed from the equatorial direction) is typical of an average SN Ia, but too fast when compared to observed SNe Ia of equivalently high peak brightness.

- The R-, I-, and J-band light curves of the model exhibit a secondary maximum which resembles qualitatively that seen in observations. The timing and prominence of the model secondary maximum differs somewhat from that seen in SN 2001el, likely due to the model's relatively large ^{56}Ni mass.

- The $B-V$ and $V-R$ color curves of the model (from $\theta = 90^\circ$) fit those of SN 2001el to within ~ 0.1 mag up to day 30 after maximum light. The U- and I-band light curves more strongly deviate from the observations, leading to a slightly poorer, but still reasonable match between the

model $U-B$, $B-I$, $V-I$, and $R-I$ color curves and observations.

- Inspection of the model spectra (from an equatorial view) each week from -7 to +25 days relative B-maximum shows good agreement with observations of the spectroscopically normal SN 1994D. The quality of fit is comparable to that of standard 1D explosion models such as W7 and the 1D delayed-detonations.

- The asymmetry of the model ejecta structure leads to intriguing orientation effects. The blueshifts of individual absorption features vary with viewing angle by more than 40% at maximum light. Moreover, depending on the viewing angle, the evolution of the expansion velocities (as measured from the minimum of the Si II 6150 absorption) accommodate the entire range of observed behaviors, from high to low velocity gradient (Benetti et al. 2005).

- Due to the asymmetrical velocity distribution of iron group elements, first the ultraviolet and later the blue part of the spectrum show substantial variation (by a factor of several) in flux absorption along different viewing angles. This leads to a significant dependence of the B-band decline rate on orientation, with Δm_{15} varying between $0.96 - 1.36$ mag. The model shows a correlation of $\Delta m_{15}(B)$ with the B-band peak magnitude, but the amplitude is twice weaker than the observed Phillips relation. Thus in the present model, the orientation effects can be considered as a possible source of dispersion in the underlying relation, at the level 0.12 mag.

- The intrinsic mild asymmetry of the model density structure, leads to a continuum polarization at maximum light of $P \lesssim 0.1\%$, somewhat lower than that typically observed. This may indicate that other effects not included in the present model (e.g., rotation) may be also required to reproduce the large scale ejecta asymmetry.

- The model shows line polarization up to a level $P \sim 2\%$ in the Si II "6150" and Ca II IR-triplet features, due to the aspherical distribution of IMEs. The line polarization is large from inclinations where the line velocities are highest, resembling the observed behavior noted in Leonard et al. (2005). However significant line polarization ($P \sim 1 - 2\%$) can also be seen from some viewing angles where the line velocities are relatively low, a characteristic that as of yet has no correspondence in observations.

- In the model, the material synthesized during the initial deflagration phase is transformed into a high velocity ($v \sim 25,000 - 35,000$ km s^{-1}) IME-rich outer shell. This shell resembles the structure considered in Kasen & Plewa (2005), but in the present case has a larger covering factor and a more irregular structure. Although not considered directly in this paper, this material offers one possibility to explain the detached, high-velocity absorption features commonly observed in early time SN Ia spectra (Mazzali et al. 2005).

The comprehensive methodology applied in this paper helped to appreciate certain deficiencies in the theoretical calculations. The failure to reproduce the Na I features in the post-maximum spectra follows from the use of an approximate alpha-network nucleosynthesis scheme lacking sodium. Similarly, the lack of calcium in the outer high-velocity IME shell is a direct consequence of the crude nuclear burning scheme used during the deflagration phase. The wrong trends noted at later time ($t_{\rm exp} > 60$ days) model colors likely indicate a breakdown of the assumptions adopted in the radiative transfer calculations, in particular the neglect of non-thermal ionization effects. Meanwhile, the poor correspondence in the model H- and K-band light curves with observations reflects, in large part, the inadequacy of the available atomic line list data.

The current Y12 model is only one example of the family of DFD explosions (Paper I). Other explosion models from that family show variations in the total ^{56}Ni mass, explosion energy, morphology and ejecta dynamics. With the addition of even more advanced physics, it is natural to expect that interesting new behaviors will emerge. Using a more realistic progenitor structure and ignition conditions may affect the nucleosynthesis in the model, thereby altering the composition of the core region, energetics of the deflagration, and overall explosion energy. That in turn is likely to influence certain model observables, such as the absolute luminosity, the dispersion in B-band decline rates, and the model continuum polarization.

A major advance of the multi-dimensional radiative transfer calculations presented in this paper is our ability to quantify the dependence of model observables on the viewing angle. We identified several intriguing orientation effects in the Y12 model which suggest specific ways in which the asphericity of SNe Ia may contribute to their photometric and spectroscopic diversity. In particular, asymmetry in the velocity distribution of iron group elements leads to a strong dependence of the B-band decline rate on viewing angle. This fact both constrains the degree of compositional asymmetry present in the ejecta of SNe Ia and points to a potential source of dispersion in the SN Ia width-luminosity relation. Although not the case for the Y12 model, one may be tempted to wonder whether a multi-dimensional SN Ia model could be imagined such that the peak luminosity variations of SNe Ia and their correlation with the light curve width might arise, at least to some degree, from an orientation effect.

The comparison of SN theory and observation faces new and interesting challenges once multi-dimensional models are considered. Given the viewing angle dependence, the predictions of aspherical models bear an intrinsic multiplicity. Model validation can then no longer be limited to the traditional exercise of matching synthetic light curves and spectra to individual SN observations. Rather, we must also study the probability distributions and dispersion levels characterizing various model observables (e.g., peak magnitudes, decline rates, line velocities and polarization levels) along with the internal correlations relating different sets of such observables. These statistical properties of the model can then be compared to those of a relevant sample of observed SNe. Although we have touched on this methodology in several places here, more generally the situation will be

further complicated by the presence of additional dimensions of diversity other than asymmetry alone. For example, the DFD and other theoretical paradigms admit a family of SN Ia models which range in ^{56}Ni mass. More extensive validation studies thus await further specificity of the theory. Equally important will be the development of massive and easily accessible observational databases containing light curves, spectra, and polarization for a large number of SNe.

The general success of the Y12 model in reproducing the basic properties of observed SNe Ia is not entirely surprising, considering that the DFD scenario represents a variation on the standard 1D delayed-detonation models which have been shown to be in fair agreement with observations (e.g., Höflich & Khokhlov 1996; Höflich 1995). Moreover, the ejecta asymmetry studied here may be generic to a broader class of SN Ia explosion models. Standard delayed-detonation models, for example, show a similar systematic offset in the ejecta compositional structure if the transition to detonation is triggered at one point off-center (Livne 1999; Gamezo et al. 2005). In such models, nuclear burning extends to higher velocity on the side of the ejecta where the detonation takes place, just the opposite of that seen in the Y12 model. Nevertheless, the overall morphologies are similar, and the models likely share many of the same photometric/spectroscopic variations and polarization signatures discussed here.

Ultimately, the viability of the DFD explosion scenario is subject to further tests of the robustness of the DFD mechanism itself once the simplifying assumption of axial symmetry is removed and when more realistic initial ignition conditions are considered. Nevertheless, the overall good agreement of the Y12 model with a broad range of SN Ia observations certainly warrants future, more in-depth investigations into the DFD and related multi-dimensional delayed-detonation scenarios. This agreement is especially impressive given that the model was not artificially manipulated in order to match observations, rather the system was evolved without intervention from the initial ignition to several months past maximum light. We believe that this sort of end-to-end methodology is critical in developing and validating future theoretical models of thermonuclear supernova explosions.

DK is supported by the Allan C. Davis fellowship at Johns Hopkins University and the Space Telescope Science Institute. This work is supported in part by the U.S. Department of Energy under Grant No. B523820 to the Center for Astrophysical Thermonuclear Flashes at the University of Chicago. This research used resources of the National Energy Research Scientific Computing Center, which is supported by the Office of Science of the U.S. Department of Energy under Contract No. DE-AC03-76SF00098.

REFERENCES

Arnett, W. D. 1969, Ap&SS, 5, 180
Baron, E., Hauschildt, P. H., Nugent, P., & Branch, D. 1996, MNRAS, 283, 297
Baron, E., Bongard, S., Branch, D., & Hauschildt, P. H. 2006, ApJ, 645, 480
Benetti, S. et al. 2005, ApJ, 623, 1011
Blinnikov, S. I., Röpke, F. K., Sorokina, E. I., Gieseler, M., Reinecke, M., Travaglio, C., Hillebrandt, W., & Stritzinger, M. 2006, A&A, 453, 229
Branch, D., Baron, E., Hall, N., Melakayil, M., & Parrent, J. 2005, PASP, 117, 545
Branch, D., Doggett, J. B., Nomoto, K., & Thielemann, F.-K. 1985, ApJ, 294, 619
Chornock, R., Filippenko, A. V., Branch, D., Foley, R. J., Jha, S., & Li, W. 2006, PASP, 118, 722
Cardelli, J. A., Clayton, G. C., & Mathis, J. S. 1989, ApJ, 345, 245
Conley, A., et al. 2006, AJ, 132, 1707
Fryxell, B. A., Müller, E., & Arnett, W. D. 1989, Max-Planck-Institut für Astrophysik, Preprint 449, (Garching: MPA)
Fryxell, B. et al. 2000, ApJS, 131, 273
Gamezo, V. N., Khokhlov, A. M., & Oran, E. S. 2005, ApJ, 623, 337
Höflich, P., & Stein, J. 2002, ApJ, 568, 779
Höflich, P., Gerardy, C. L., Fesen, R. A., & Sakai, S. 2002, ApJ, 568, 791
Hamuy, M., Phillips, M. M., Suntzeff, N. B., Schommer, R. A., Maza, J., & Aviles, R. 1996, AJ, 112
Harkness, R. 1991, in Supernova 1987A and other supernovae, ESO Conference and Workshop Proceedings, Proceedings of an ESO/EIPC Workshop, Marciana Marina, Isola d'Elba, September 17-22, 1990, Garching: European Southern Observatory (ESO), —c1991, edited by I. J. Danziger, and Kurt Kjär., p.447, 447–+
Höflich, P., & Khokhlov, A. 1996, ApJ, 457, 500
Höflich, P. 1995, ApJ, 443, 89
Höflich, P., Khokhlov, A. M., & Wheeler, J. C. 1995, ApJ, 444, 831
Howell, D. A., Höflich, P., Wang, L., & Wheeler, J. C. 2001, ApJ, 556, 302
Jeffery, D. J., Leibundgut, B., Kirshner, R. P., Benetti, S., Branch, D., & Sonneborn, G. 1992, ApJ, 397, 304
Kasen, D. 2006, ApJ, 649, 939
Kasen, D. et al. 2003, ApJ, 593, 788
Kasen, D., & Plewa, T. 2005, ApJ, 622, L41
Kasen, D., & Woosley, S. 2007, ApJ in Press
Kasen, D., Thomas, R. C., & Nugent, P. 2006, ApJ, 651, 366
Khokhlov, A. 1994, ApJ, 424, L115
Khokhlov, A. M, Oran, E. S., & Wheeler, J. C. 1997, ApJ, 478, 678
Krisciunas, K. et al. 2003, AJ, 125, 166
Lentz, E. J., Baron, E., Branch, D., & Hauschildt, P. H. 2001, ApJ, 557, 266
Leonard, D. C., Li, W., Filippenko, A. V., Foley, R. J., & Chornock, R. 2005, ApJ, 632, 450
Wang, L., et al. 2006, ApJ submitted, astro-ph/0409593
Livne, E. 1999, ApJ, 527, L97
Mazzali, P. A. et al. 2005, ApJ, 623, L37
Meikle, W. P. S., et al. 1996, MNRAS, 281, 263
Nobili, S. et al. 2005, A&A, 437, 789
Nomoto, K., Thielemann, F., & Yokoi, K. 1984, ApJ, 286, 644
Nugent, P., Baron, E., Branch, D., Fisher, A., & Hauschildt, P. H. 1997, ApJ, 485, 812
Patat, F., et al. 1996, MNRAS, 278, 111
Phillips, M. M., Lira, P., Suntzeff, N. B., Schommer, R. A., Hamuy, M., & Maza, J. 1999, AJ, 118, 1766
Pinto, P. A., & Eastman, R. G. 2001, New Astronomy, 6, 307
Plewa, T. 2007, ApJ in press, astro-ph/0611776 (Paper I)
Reinecke, M., Hillebrandt, W., & Niemeyer, J. C. 2002, A&A, 391, 1167
Riess, A. G. et al. 1999a, AJ, 118, 2675
—. 1999b, AJ, 117, 707
Swartz, D. A. 1991, ApJ, 373, 604
Wang, L. et al. 2003, ApJ, 591, 1110
Wheeler, J. C., Höflich, P., Harkness, R. P., & Spyromilio, J. 1998, ApJ, 496, 908